Low Reynolds number flow over non-rectangular bluff bodies

Mr. Evan Fernandes[1]

UG Student, Department of Aerospace Engineering

[1]Amity University Mumbai, Mumbai

Mr. Nishit Pachpande[2], Mr. Biraj Khadka[3], Dr. Tushar Chourushi[4]

[2]FOSSEE, IIT Bombay, Mumbai, Maharashtra, India

[3]FOSSEE, IIT Bombay, Mumbai, Maharashtra, India

[4] Department of Aerospace Engineering, MIT Art, Design and Technology University, Pune, Maharashtra 412201, India

Synopsis

This study presents a comprehensive transient numerical analysis of the flow around a 2D bluff body using OpenFOAM, a robust open-source computational fluid dynamics (CFD) software. The investigation focuses on understanding the behaviour of low Reynolds number flows over bluff bodies, specifically using the PISOFoam solver (OpenFOAM, toolkit). The accuracy of the solver was initially verified against established research findings on rectangular bluff bodies operating under low Reynolds numbers. The study systematically explores the influence of angle of attack (AOA) on flow characteristics, at a Reynolds number of 150. Multiple angles of attack ranging from 0° to 30° were simulated to capture the diverse aerodynamic responses of the bluff bodies (blunt-headed and elliptical). Key parameters such as lift coefficient (C_L), drag coefficient (C_D), Strouhal number, and velocity contours were meticulously analysed to uncover insightful trends and phenomena. Results revealed distinct patterns in the variation of lift and drag coefficients across different AOAs, highlighting the complex interaction between flow separation, vortex shedding, and wake dynamics. The fluctuating nature of these coefficients underscored the unsteady nature of the flow, influenced significantly by the changing AOA. Notably, the Strouhal number computations vividly illustrated the periodic shedding of vortices in the wake region, emphasizing the body's aerodynamic instability. Visual representations through pressure and velocity contours provided a clear depiction of flow structures and boundary layer characteristics, offering valuable insights into flow behaviour around bluff bodies. These contours served as essential tools in identifying regions of high and low-pressure gradients, thereby enhancing the understanding of flow separation and reattachment phenomena. Overall, this study contributes significantly to advancing our comprehension of bluff body aerodynamics using CFD. By exploring a range of AOAs and rigorously analyzing key parameters, the research deepens insights into flow behaviour under low Reynolds number conditions. The findings not only validate the computational approach but also enrich the broader knowledge of flow physics, benefiting applications in aerodynamic design, wind engineering, and vehicle performance optimization.

Keywords: blunt-headed bluff body, elliptical bluff body, PISOfoam solver, Reynolds number, openFOAM

1. Introduction

Bluff bodies, distinguished by their non-streamlined shapes and sharp edges, are fundamental to numerous engineering disciplines and natural systems. These structures disrupt the flow of fluid around them, leading to complex phenomena such as flow separation, vortex shedding, and turbulence. Understanding these phenomena is crucial for optimizing design and performance across a wide array of applications, from civil engineering and automotive design to environmental management and aerospace engineering. Fig. 1 shows the complex flow behaviour past various shapes taken from the existing reference [4].
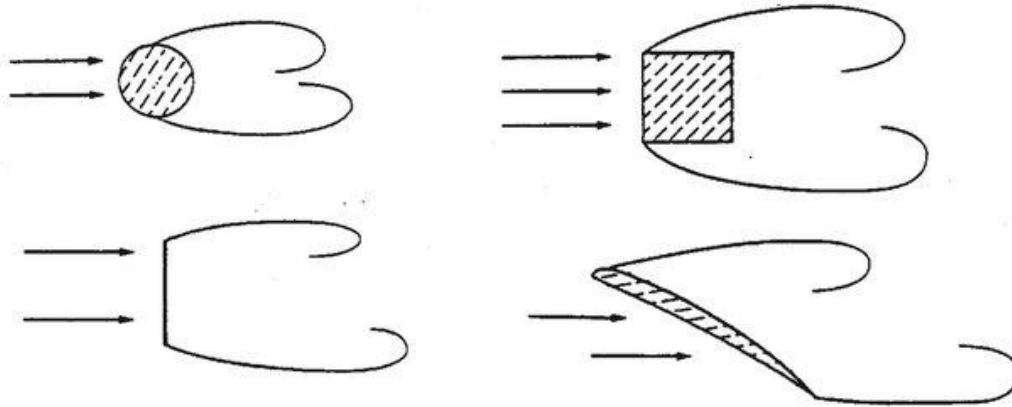

Fig. 1. Examples of aerodynamic and bluff bodies [4]

In civil engineering, for example, the stability and safety of buildings and bridges are heavily influenced by wind loads, which are affected by the turbulent wakes generated by bluff bodies. Similarly, in the automotive and aerospace industries, drag reduction is a primary concern, where the design of vehicles and aircraft must consider the impact of bluff body components to enhance fuel efficiency and performance. Environmental studies also rely on the understanding of flow around bluff bodies to predict the dispersion of pollutants and the behaviour of natural formations like rock outcrops and trees.

Despite significant advancements in fluid dynamics, the flow around non-rectangular bluff bodies, particularly at low Reynolds numbers and varying angles of attack, remains an area with limited understanding. Most existing studies have focused on simple geometries such as circular and square cylinders, and primarily under high Reynolds number conditions. These studies, while valuable, do not fully capture the diversity of real-world scenarios where the geometry of bluff bodies can be far more complex, and flow conditions can vary widely.

1.1 Literature Review

The study by Yuce M. et al. [2] offers a detailed examination of the flow behaviour around two-dimensional (2D) circular and square cylinders at various Reynolds numbers, contributing valuable insights to the literature on fluid dynamics. Using numerical simulations, this research explored flow fields around cylinders with identical characteristic lengths under consistent flow conditions, covering a Reynolds number range from laminar (Re = 2) to highly turbulent (Re = 4×10^6). The simulations employed the shear stress transport (SST) k-omega turbulence model and were conducted using commercial software. Results from these simulations showed excellent agreement with existing literature, reinforcing their validity. The findings highlight the significant impact of cylinder shape on the flow field. Specifically, under the same initial conditions, the wake downstream of the square cylinder was found to be considerably more turbulent than that of the circular cylinder. Furthermore, as the Reynolds number increased, the turbulence intensity in the wake flow also increased, and the wake's length downstream of both cylinders extended. This study underscores the critical role of geometric factors in influencing flow characteristics and provides a robust foundation for further research in this domain.

The study by Chatterjee D. et al. [3] explores the interaction between uniform free stream flow and the flow induced by the rotation of a sharp-edged body through numerical investigation. A two-dimensional (2D) finite volume-based approach is employed to simulate the laminar flow around a rotating square cylinder in an unconfined medium. The study utilizes a body-fitted grid system with moving boundaries to solve the incompressible Navier–Stokes equations. The Reynolds number (Re) based on the free stream flow is varied from 10 to 200, while the dimensionless rotational speed (Ω) of the cylinder ranges from 0 to 5 [3]. At a low Re of 10, the flow field remains steady regardless of the rotational speed. For Re values between 50 and 200, regular low-frequency Karman vortex shedding (VS) is observed up to a critical rotational speed (Ωcr). Beyond this critical speed, the global flow becomes steady, although high-frequency oscillations in aerodynamic coefficients are noted. Similar degeneration of Karman VS is observed for a rotating circular cylinder at certain critical rotational speeds, though notable differences emerge at higher rotational speeds. This study is pioneering in reporting the fluid dynamic behaviour around a rotating square cylinder in an unconfined free stream flow, providing new insights into the complex interactions in such systems.

Therefore, it can be reasonably concluded that there is a lack of existing research on the flow over non-rectangular bluff bodies at a low Reynolds number (Re = 150) and varying angles of attack [5]. This research intends to fill this gap in the current body of knowledge. In the current numerical investigation, the flow characteristics around non-rectangular bluff bodies at low Reynolds numbers and different angles of attack have been examined using the open-source CFD software, OpenFOAM.

1.2 Fluid flow parameters

Fluid flow parameters are essential for comprehending and analyzing the behaviour of fluid flow processes. In the context of the present study, various non-dimensional numbers and coefficients have been examined. The details are provided below.

1.2.1 Reynolds Number

The Reynolds number is a crucial dimensionless parameter in fluid mechanics, used to characterize the flow regime of a fluid and predict the transition from laminar to turbulent flow [4]. Named after the Irish engineer Osborne Reynolds, who first studied this phenomenon, the Reynolds number (*Re*) is defined as the ratio of inertial forces to viscous forces in a fluid flow. It is calculated using the following formula:

$$Re = \frac{UL}{\nu}$$

where U is the velocity, L is the characteristic length, and ν is the kinematic viscosity of the fluid.

The Reynolds number is significant because it helps determine the flow regime, providing insight into whether the fluid will exhibit smooth, orderly laminar flow or chaotic, turbulent flow. This parameter is crucial in understanding fluid behaviour and is particularly important in the study of flow around bluff bodies. It influences key aerodynamic characteristics such as drag, lift, and the overall stability of the flow.

In fluid dynamics, the Reynolds number assists in predicting the transition point from laminar to turbulent flow, which can have profound effects on the aerodynamic properties of bluff bodies. Higher Reynolds numbers typically indicate a tendency toward turbulence, affecting the flow separation points, wake formation, and vortex shedding patterns. Consequently, understanding the Reynolds number is essential for optimizing the design and performance of structures and vehicles subjected to fluid flow, as it directly impacts drag forces and aerodynamic efficiency.

1.2.2 Lift and Drag Coefficients

In fluid dynamics, drag refers to the resistive force that acts opposite to the relative motion of an object moving through a fluid. This phenomenon occurs due to the interaction between the fluid and the object's surface. Unlike other forms of resistance, such as dry friction, drag forces are velocity-dependent. In laminar flow, the drag force is proportional to the velocity, while in turbulent flow, the drag force is proportional to the square of the velocity.

Although viscous friction is a primary contributor to drag, turbulent drag is largely independent of the fluid's viscosity.

The drag coefficient (C_D) is a dimensionless number used to quantify the drag or resistance of an object in a fluid environment. It is defined as the ratio of the drag force to the product of the dynamic pressure of the fluid and the reference area. The drag coefficient is typically determined through experimental methods and varies with the object's shape and flow conditions. For instance, a streamlined object with a smooth surface will exhibit a lower drag coefficient compared to an irregular or rough object. The drag coefficient formula is given by:

$$C_D = \frac{2F_D}{\rho U^2 A}$$

where F_D is the drag force, ρ is the fluid density, U is the fluid velocity, and A is the reference area.

Lift, on the other hand, is the force that acts perpendicular to the direction of motion, opposing the weight of an object. This force is generated by the pressure difference between the upper and lower surfaces of the object, such as an aeroplane wing or a kite. The shape of the object, its velocity, and the fluid's density and viscosity all influence the amount of lift generated. According to Bernoulli's principle, an increase in fluid velocity results in a decrease in pressure. The curved upper surface of a wing causes the air to flow faster over the top, creating a lower pressure area and generating lift.

The lift coefficient (C_L) is another dimensionless number used to describe the lift force acting on an object moving through a fluid. It is defined as the ratio of the lift force to the product of the dynamic pressure of the fluid and the reference area. The lift coefficient is crucial in aerodynamics and fluid dynamics for quantifying the lift experienced by objects such as wings and airfoils. The lift coefficient formula is given by:

$$C_L = \frac{2F_L}{\rho U^2 A}$$

Where F_L is the lift force, ρ is the fluid density, U is the fluid velocity, and A is the reference area.

In summary, the drag coefficient (C_D) and lift coefficient (C_L) are vital for understanding and predicting the aerodynamic performance of objects in fluid flow. These coefficients allow engineers and scientists to design and optimize various structures, from vehicles to buildings, ensuring they meet performance and efficiency requirements.

1.2.3 Strouhal Number

The Strouhal number is a dimensionless parameter used in fluid dynamics to describe the unsteady behaviour of fluid flow around an object [4]. It quantifies the relationship between the frequency of vortex shedding or oscillations in the flow and the flow velocity, along with a characteristic length scale of the object. Named after the Czech physicist Vincenc Strouhal, who first identified this relationship, the Strouhal number is a critical factor in understanding fluid dynamics around bluff bodies. Mathematically, the Strouhal number (St) is expressed as:

$$St = \frac{fL}{U}$$

Where f represents the frequency of vortex shedding or flow oscillations, L is a characteristic length scale of the object (such as its diameter or width), and U is the flow velocity.

The Strouhal number is instrumental in providing insights into the unsteady nature of fluid flows, particularly around bluff bodies like cylinders or aerofoils. It is widely used to predict phenomena such as flow-induced vibrations, acoustic effects, and vortex-shedding patterns behind objects. Understanding the Strouhal number helps engineers and scientists anticipate the dynamic behaviour of fluids, which is crucial for the design and analysis of various structures exposed to fluid flow.

2. Governing Equations and Models

The fluid flow in this study is assumed to be turbulent, two-dimensional, and unsteady. Despite the relatively low flow velocity, which typically would not lead to significant density variations in the working fluid, the flow is treated as compressible. The Shear Stress Transport (SST) k-ω turbulence model is employed. This model, a widely used Reynolds-Averaged Navier-Stokes (RANS) turbulence model, effectively merges the strengths of both the k-epsilon and k-omega models. It provides enhanced accuracy for predicting a broad spectrum of flows, particularly those involving both attached and separated turbulent boundary layers. The fluid's physical properties, such as viscosity and density, are assumed to correspond to the characteristics of air. In this investigation, the flow and energy equations are solved separately. The governing differential equations that underpin this study are formulated as follows.

Conservation of Mass (Continuity Equation):

$$\frac{\partial \rho}{\partial t} + \frac{\partial (\rho U)}{\partial x} + \frac{\partial (\rho V)}{\partial y} = 0$$

Conservation of Momentum (Momentum Equations):

X -momentum –

$$\frac{\partial (\rho U)}{\partial t} + U \frac{\partial (\rho U)}{\partial x} + V \frac{\partial (\rho U)}{\partial y} = -\frac{\partial P}{\partial x} + \mu_{eff} \left(\frac{\partial^2 U}{\partial x^2} + \frac{\partial^2 U}{\partial y^2} \right) + \rho g_x$$

Y -momentum –

$$\frac{\partial (\rho V)}{\partial t} + U \frac{\partial (\rho V)}{\partial x} + V \frac{\partial (\rho V)}{\partial y} = -\frac{\partial P}{\partial y} + \mu_{eff} \left(\frac{\partial^2 V}{\partial x^2} + \frac{\partial^2 V}{\partial y^2} \right) + \rho g_y$$

Energy Equation:

$$\frac{\partial (\rho E)}{\partial t} + U \frac{\partial (\rho UH)}{\partial x} + V \frac{\partial (\rho VH)}{\partial y} = -\frac{\partial (PU)}{\partial y} - \frac{\partial (PV)}{\partial y} + k \left(\frac{\partial^2 T}{\partial x^2} + \frac{\partial^2 T}{\partial y^2} \right) + Q$$

Turbulence Model Equations (k-omega SST RANS):

Transport Equation for Turbulent Kinetic Energy (k) –

$$\frac{\partial (\rho k)}{\partial t} + \frac{\partial (\rho kU)}{\partial x} + \frac{\partial (\rho kV)}{\partial y} = \frac{\partial}{\partial x} \left[\left(\mu + \frac{\mu_t}{\sigma_k} \right) \frac{\partial k}{\partial x} \right] + \frac{\partial}{\partial y} \left[\left(\mu + \frac{\mu_t}{\sigma_k} \right) \frac{\partial k}{\partial y} \right] + P_k - \beta \rho k \omega$$

Transport Equation for Specific Dissipation Rate (ω) –

$$\frac{\partial (\rho \omega)}{\partial t} + \frac{\partial (\rho \omega U)}{\partial x} + \frac{\partial (\rho \omega V)}{\partial y} = \frac{\partial}{\partial x} \left[\left(\mu + \frac{\mu_t}{\sigma_\omega} \right) \frac{\partial \omega}{\partial x} \right] + \frac{\partial}{\partial y} \left[\left(\mu + \frac{\mu_t}{\sigma_\omega} \right) \frac{\partial \omega}{\partial y} \right] + \alpha P_k - \beta \rho \omega^2 + 2(1 - F1) \frac{\rho \sigma}{\omega}$$

In the given context, ρ denotes the density of air, while t represents time. The velocity components in the x and y directions are indicated by u and v respectively. The symbol p stands for pressure. The term μ_{eff} signifies effective viscosity, which is a combination of molecular viscosity and turbulent viscosity. The components of acceleration in the x and y directions are denoted by g_x and g_y respectively. E refers to the total energy per unit volume, k is the turbulent kinetic energy and ω represents the specific dissipation rate. The term P_k describes the production rate of turbulent kinetic energy. The model constants are represented by β, and μ_t stands for the turbulent viscosity. The empirical blending function $F1$ is used to transition between different regions of the flow, typically depending on the flow conditions or the distance from the wall. Lastly, σ is the turbulent Prandtl number, which is associated with the diffusion of ω and k.

3. Simulation Procedure

3.1 Geometry and Mesh

The geometric configurations and empirical dimensions for the two cases, a blunt-headed body and an elliptical body, are depicted in Figures 2 and 3, respectively.

3.1.1 Blunt-Headed Body Configuration

In the first scenario, a fixed, two-dimensional blunt-headed object is immersed in a uniform free-stream flow with velocity U. The blunt-headed bluff body features a diameter of D and an overall length of 1.5D. The computational domain encompassing this body extends 60D in length and 20D in height, ensuring sufficient space to capture flow phenomena. The upstream section is 15D in length, providing adequate development length for the incoming flow, while the downstream section spans 45D to capture the wake and flow reattachment. The origin of the coordinate system is situated at the geometric centre of the circular section of the blunt-headed body, with drag force oriented positively in the x-direction and lift force oriented positively in the y-direction.
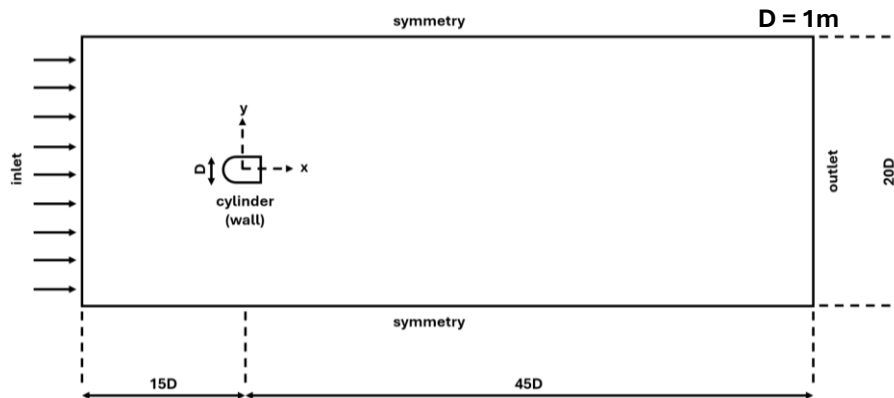
Fig. 2. Physical domain for Case 1 (blunt-headed body)

3.1.2 Elliptical Body Configuration

In the second scenario, a fixed, two-dimensional elliptical body is subjected to the same uniform free-stream flow with velocity U. The elliptical body has a major axis length of D and a minor axis length of 0.5D. The computational domain dimensions are maintained at 60D in length and 20D in height, consistent with the blunt-headed case. Similarly, the upstream and downstream lengths are 15D and 45D, respectively, to ensure comprehensive capture of flow dynamics. The geometric centre of the elliptical body serves as the origin of the coordinate system, with the same orientation for the drag and lift forces as defined in the blunt-headed body configuration.
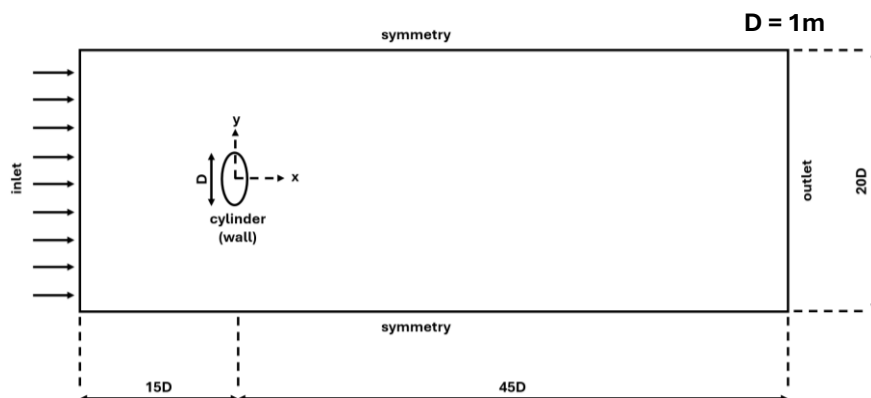

Fig. 3. Physical domain for Case 2 (elliptical body)

3.1.3 Meshing and Numerical Analysis

The meshing for both configurations, as shown in Figures 2 and 3, is meticulously designed using ANSYS Fluent to capture the fine details of fluid interaction around the bodies. A refined mesh near the body surfaces and in the wake regions ensures accurate resolution of boundary layers and vortex shedding phenomena. This setup allows for a detailed comparison of flow characteristics between the blunt-headed and elliptical bodies, providing valuable insights into how different geometries influence aerodynamic properties such as drag and lift forces under identical flow conditions. The mesh for the blunt-headed body (fig. 4) consists of a total of 42,200 hexahedral cells. It has a maximum aspect ratio of 4.60281 and a maximum skewness of 2.46928, tailored specifically to accommodate the unique geometry and aerodynamic characteristics of the blunt-headed design. For the elliptical body (fig.5), the mesh is composed of 36,800 hexahedral cells. This mesh configuration has a maximum aspect ratio of 6.40251 and a maximum skewness of 1.97311, optimized to match the smooth contours and flow dynamics associated with an elliptical shape.
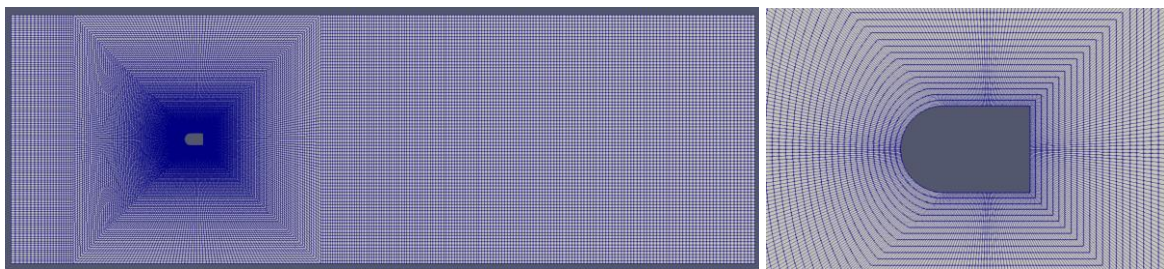
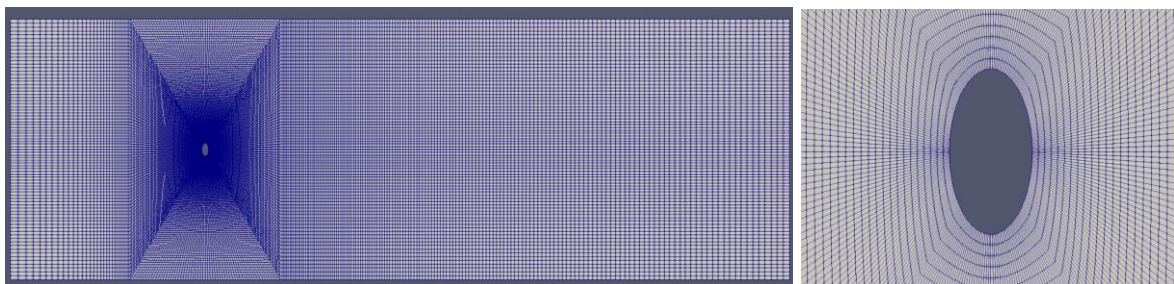Fig. 4. Mesh of the computational domain for Case 1 (blunt-headed body)

Fig. 5. Mesh of the computational domain for Case 2 (elliptical body)

3.1.4 Angle of Attack Simulation

For both configurations, the inlet velocity is varied to simulate angles of attack ranging from 0 degrees to 30 degrees, with increments of 10 degrees. Thus, simulations are conducted at angles of 0, 10, 20, and 30 degrees. This approach allows for a comprehensive analysis of how the flow dynamics and aerodynamic forces change with different orientations of the bodies relative to the incoming flow.

By analyzing these configurations, the study aims to deepen the understanding of how shape and flow dynamics interact, which is crucial for optimizing design and performance in various engineering applications. The results are expected to highlight significant differences in wake structures, vortex shedding frequencies, and force coefficients, contributing to the broader field of fluid dynamics research.

3.2 Initial and Boundary Conditions

The initial and boundary conditions for both cases are listed below in Table 1.

Table 1. Boundary Conditions for Cases 1 and 2

Boundary Conditions	Region	Patch	Type	Value
U	fluid	inlet	fixedValue	uniform (U 0 0)
		outlet	zeroGradient	-
		symmetry	zeroGradient	-
		cylinder	noSlip	-
p	fluid	inlet	zeroGradient	-
		outlet	zeroGradient	-
		symmetry	zeroGradient	-
		cylinder	zeroGradient	-
k	fluid	inlet	turbulentIntensityKineticEnergyInlet	uniform- 0.0108
		outlet	zeroGradient	-
		symmetry	zeroGradient	-
		cylinder	kqRWallFunction	uniform 0.0108
omega	fluid	inlet	turbulentMixingLengthFrequencyInlet	uniform 2.715
		outlet	zeroGradient	-
		symmetry	zeroGradient	-
		cylinder	omegaWallFunction	uniform 2.715

This table outlines the boundary conditions for a fluid dynamics simulation, focusing on four key patches: inlet, outlet, symmetry, and cylinder. For velocity (U), the inlet has a fixed uniform value (U 0 0), indicating a steady inflow, while the outlet and symmetry patches use zeroGradient, meaning no velocity change across these boundaries. The cylinder patch employs a noSlip condition, indicating zero velocity at the cylinder's surface. For pressure (p), all patches use zeroGradient, signifying no pressure change across these boundaries. For turbulent kinetic energy (k), the inlet uses a turbulentIntensityKineticEnergyInlet condition with a value of 0.0108, defining the turbulence level at entry, while the outlet and symmetry patches are zeroGradient. The cylinder patch uses kqRWallFunction with the same value for wall turbulence modelling. For the specific dissipation rate (ω), the inlet applies a turbulentMixingLengthFrequencyInlet condition with a value of 2.715 to set the frequency of turbulent eddies, while the outlet and symmetry patches remain zeroGradient. The cylinder uses omegaWallFunction with the same value to handle wall effects. These conditions ensure precise modelling of flow dynamics and turbulence within the simulation domain.

To establish initial and boundary data for turbulence, we need to define the turbulence intensity (I). This dimensionless quantity is the ratio of the magnitude of turbulent fluctuations to the magnitude of the characteristic mean velocity [6].

$$I = 0.16 \, Re^{-\frac{1}{8}}$$

Turbulence intensity typically ranges from 0 to 20. An intensity value between 0 and 1 indicates low turbulence, 1 to 5 signifies medium turbulence, and 5 to 20 represents high turbulence [6]. Accurate measurements of turbulent fluctuations can be obtained using fluid dynamics experimental equipment. For fully developed pipe flow, we can employ the appropriate relation for turbulence intensity.

$$k = \frac{3}{2}\left(U_{ref} \times I\right)^2$$

For the specific dissipation rate ω, we have

$$\omega = \frac{\sqrt{k}}{C_\mu^{\frac{1}{4}} \times l}$$

Here, C_μ = 0.09, whereas l = 0.07 × L. Here L is the characteristic length of the bluff body (L = 1). Based on the Reynolds number and freestream velocity (U), the turbulence intensity (k) and specific dissipation rate (ω) change [6].

3.3 Solver

In this study, we use OpenFOAM v9 with the 'pisoFoam' solver to simulate transient, incompressible, and turbulent flow scenarios. We used the pisoFoam solver (in OpenFOAM) for addressing transient, incompressible, and turbulent flow problems using the PISO (Pressure-Implicit with Splitting of Operators) algorithm [7]. As a transient solver, pisoFoam is designed to handle time-dependent simulations, making it ideal for scenarios where fluid flow changes over time. It is particularly suited for incompressible flows, where the fluid density remains constant, a common assumption in many engineering applications. The solver's ability to manage turbulent flow is crucial for accurately modelling real-world fluid dynamics, as turbulence plays a significant role in many practical flow situations. The convective terms are solved using the higher-order numerical schemes and other terms are discretized using the central difference techniques [8]. The unsteady terms are discretized using the first-order Euler scheme [9] and all other solver settings are adjusted based on the references [7-10].

The pisoFoam solver finds applications across various fields. In environmental engineering, it is used to simulate the dispersion of pollutants in air and water, helping to assess environmental impact and devise mitigation strategies. In the automotive industry, pisoFoam models airflow over vehicle bodies to optimize aerodynamics, enhancing fuel efficiency and performance. Aerospace engineers rely on it to analyse airflow around aircraft wings and fuselages, aiding in the design of more efficient and stable aircraft. Civil engineers use the solver to study wind loads on buildings and bridges, ensuring structural safety and integrity. Additionally, in biomedical engineering, pisoFoam is employed to simulate blood flow in arteries and around medical devices, contributing to the development of effective treatments and medical interventions.

Despite its versatility, pisoFoam has certain limitations. Transient simulations, particularly those involving high-resolution meshes and complex turbulence models, can be computationally intensive, requiring significant resources and time. Setting accurate boundary conditions can be challenging, and incorrect specifications may lead to erroneous results. The solver may encounter numerical stability issues, especially in highly turbulent or complex flow scenarios, necessitating careful attention to numerical schemes and solver settings. Moreover, pisoFoam is specifically designed for incompressible flows and is not suitable for compressible flow simulations, which require different solvers and algorithms. Understanding these limitations is essential for effectively utilizing pisoFoam and obtaining reliable simulation outcomes.

3.3.1 Case Setup in pisoFoam

The folder structure for both cases is listed below in Table 2.

Table 2. Folder structure of pisoFoam solver in OpenFOAM V9

0/: folder	
│ --	- k
	- nut
	- omega
	- p
	- U

constant/: folder		
│ ------------------ polyMesh/: folder		
	│ ----------------	- boundary
		- cellZones
		- faces
		- faceZones
		- neighbour
		- owner
		- points
		- pointZones
│ ---		- transportProperties
		- turbulenceProperties

system/: folder	
│ --	- controlDict
	- decomposeParDict
	- fvSchemes
	- fvSolution

In this study, we use OpenFOAM v9 with the 'pisoFoam' solver to simulate transient, incompressible, and turbulent flow scenarios. Each folder within the case directory plays a specific role in setting up and executing the simulation.

The '0' directory is dedicated to the initial conditions for the simulation. It contains files such as 'k' for the initial turbulent kinetic energy, 'omega' for the initial specific dissipation rate, 'nut' for the initial turbulent kinematic viscosity, 'p' for the initial pressure field, and 'U' for the initial velocity field. These files are crucial for defining the starting state of the fluid flow within the simulation domain.

The `constant` directory houses files that define the fixed properties and boundary conditions of the simulation. Within this directory, 'transportProperties' specifies the transport models and properties of the fluids involved, while 'turbulenceProperties' outlines the turbulence model parameters. The 'polyMesh' subdirectory includes essential mesh files such as 'boundary', which details the types and locations of boundary patches; 'cellZones', which delineates different regions within the mesh; and connectivity files like 'faces', 'neighbour', and 'owner', which describe the relationships between mesh elements. The 'points' file lists the coordinates of the mesh vertices, establishing the geometric framework of the simulation.

In the 'system' directory, key configuration files manage the overall simulation setup. The 'controlDict' file defines global simulation controls, including the start and end times, time step size, and output intervals. 'decomposeParDict' is used for setting up domain decomposition for parallel processing, enhancing computational efficiency. The 'fvSchemes' file specifies the numerical schemes applied to discretize the governing equations, while 'fvSolution' contains solver settings and relaxation factors to ensure numerical stability and convergence.

During the simulation, a 'postProcessing' directory is created to store the results. This directory organizes data from the simulation, facilitating analysis and visualization of the flow characteristics.

This directory structure and file organization ensure a coherent and efficient simulation process using the 'pisoFoam' solver in OpenFOAM v9, allowing for accurate and detailed modelling of transient, incompressible, and turbulent fluid flows.

3.3.2 Courant number for CFD simulations

In computational fluid dynamics (CFD), the Courant number, also known as the CFL number, is a critical dimensionless parameter that influences the stability and accuracy of numerical simulations of fluid flow. Named after the French mathematician Maurice Courant, it characterizes the relationship between the local convective time step and the local physical time step.

The Courant number is defined as the ratio of the local velocity magnitude to the grid spacing, scaled by the time step used in the simulation [5]. It is given by the formula:

$$C = \frac{U \times \Delta t}{\Delta x}$$

Where is the Courant number, U is the local velocity magnitude or the maximum velocity within the computational domain, Δt is the simulation time step, and Δx is the grid spacing or characteristic length in the computational domain. This parameter quantifies how far a fluid element can travel during a single time step relative to the size of the grid cells.

The Courant number is a key factor in determining the time step size required to accurately resolve the transient behaviour of fluid flow, especially in simulations using explicit time integration schemes. For the pisoFoam solver in OpenFOAM, which is designed for transient, incompressible, and turbulent flow problems, the Courant number is particularly significant [10]. Ensuring an appropriate Courant number is vital for maintaining the stability and accuracy of the simulation. If the Courant number is too high, the numerical solution may become unstable, leading to oscillations and erroneous results. Conversely, a very low Courant number results in excessively small time steps, increasing the computational cost without necessarily improving accuracy.

The suitable value of the Courant number depends on the specific flow conditions and the numerical method being used. Generally, for the pisoFoam solver, a Courant number of less than or equal to 1 is recommended to ensure stability when using explicit time integration methods. However, in some scenarios, slightly higher Courant numbers can be employed to enhance computational efficiency, provided that the stability and accuracy of the simulation are not compromised. Thus, managing the Courant number effectively is essential in CFD simulations with pisoFoam, balancing between computational cost and the reliability of the simulation results.

3.4 Solver Validation

The study by Yuce M. et al. [2] provides a comprehensive analysis of flow behaviour around two-dimensional (2D) circular and square cylinders at various Reynolds numbers, offering significant contributions to fluid dynamics research. Adapting the parameters from this study, simulations are conducted using OpenFOAM V9, despite the original use of a commercial solver. Given the low Reynolds numbers for the non-rectangular bluff bodies as detailed in the paper, the simpleFoam solver is utilized. simpleFoam is designed for steady-state, incompressible, turbulent flow and employs the SIMPLE (Semi-Implicit Method for Pressure-Linked Equations) algorithm, a common method for solving the Navier-Stokes equations for incompressible flows. The simulation setup includes a domain length of 65 meters and a cylinder diameter of 1 meter. The drag coefficient (CD) results are obtained for Reynolds numbers 15, 38, and 160 and are subsequently compared with the findings from the existing literature [2] in Table 3.

Table 3. Comparison of results for literature [2]

Re	Total Force N (present)	Total Force N [2]	C_D (present)	C_D [2]	Relative Difference %
15	2.92×10^{-10}	3.8×10^{-7}	3.28068	3.37	2.67
38	1.55×10^{-9}	1.52×10^{-6}	2.41403	2.1	14.95
160	2.35×10^{-8}	2.05×10^{-5}	1.86211	1.6	16.37
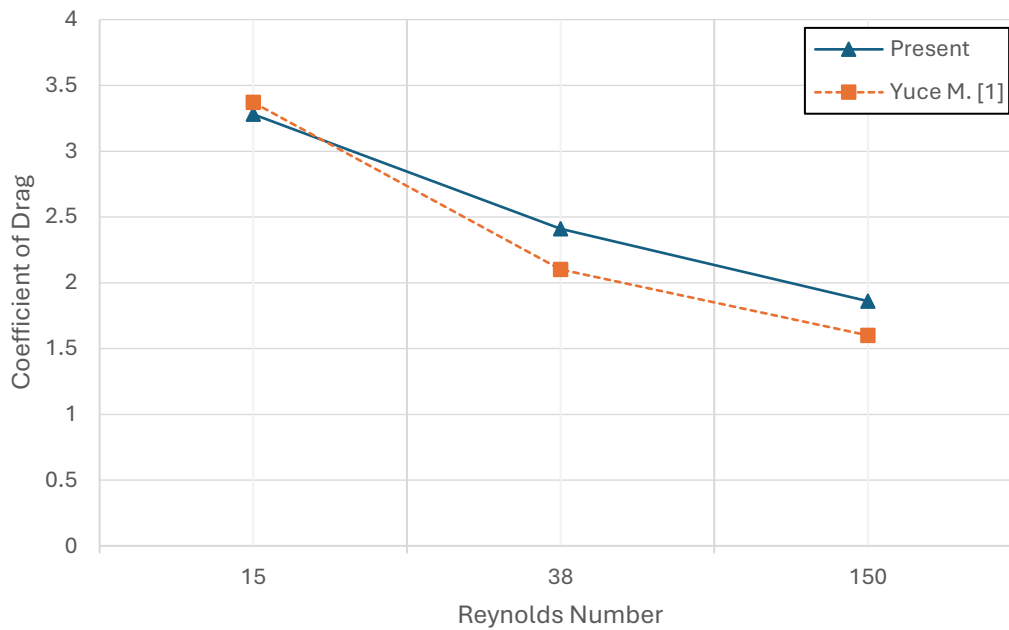
Fig. 6. Variation of Drag coefficient with Re, comparison of present values with results obtained by Yuce M. et al. [1]

The comparison for C_D and St, with the literature [3] for Re = 150 and at 0 rotational speed is listed in Table 4. The present obtained results are in close agreement with those listed in the literature with a mean variation of 52.37% in the Strouhal number and 10.63% in the drag coefficient.

Table 4. Comparison of C_D and St results for literature [3]

	St	C_D
Present	0.2441	1.77
Chatterjee D [3]	0.1602	1.6
Relative Difference (%)	52.37	10.63

4. Results and Discussions

In this research migration project, we focus on key fluid flow parameters such as the Lift Coefficient, Drag Coefficient, and Strouhal Number. These parameters are obtained for a Reynolds number of 150 and at angles of attack of 0°, 10°, 20°, and 30°. The analysis is conducted for both blunt-headed bluff bodies and elliptical bluff bodies. Logical conclusions have been drawn regarding the variation of these parameters with changes in Reynolds number and angle of attack.

4.1 Lift and Drag Coefficient

The forces acting on both the blunt-headed bluff body and the elliptical body are influenced by normal and shear stresses in the lateral and axial directions. Lift forces are measured laterally, while drag forces are determined by projecting these forces along the streamwise direction. In dynamic steady-state conditions, both drag and lift forces fluctuate due to the intermittent shedding of vortices around the bodies. To account for these fluctuations, all values are recorded at t = 100 seconds for consistency.
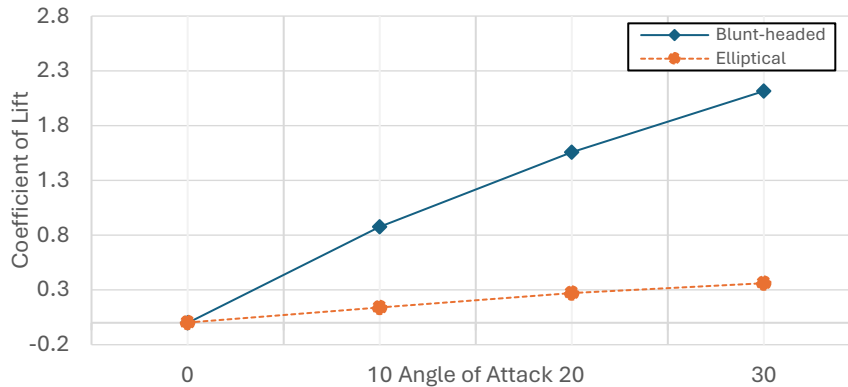
Fig. 7. Variation of Lift coefficient with Angle of attack for blunt-headed and elliptical bluff body

Figure 7 depicts the variation of the lift coefficient with the angle of attack for both blunt-headed and elliptical bluff bodies, with the Reynolds number consistently set at 150. This setup allows for a direct comparison of how each body shape responds to changes in the angle of attack under the same flow conditions. For the blunt-headed bluff body, there is a significant increase in the lift coefficient as the angle of attack rises. At 0 degrees, the lift coefficient starts at approximately zero. As the angle of attack increases to 30 degrees, the lift coefficient climbs dramatically to around 2.6. This sharp rise indicates that the blunt-headed bluff body is highly sensitive to changes in the angle of attack, resulting in a substantial increase in lift. In contrast, the elliptical bluff body shows a more gradual increase in the lift coefficient. Starting from approximately zero at a 0-degree angle of attack, the lift coefficient for the elliptical body reaches only about 0.4 when the angle of attack is increased to 30 degrees. This gradual change suggests that the elliptical bluff body experiences a more moderate increase in lift with increasing angle of attack, highlighting a less pronounced sensitivity compared to the blunt-headed body.

The differences in the lift behaviour between the two body shapes are due to their geometries, which affect the flow separation and vortex-shedding characteristics around them. By maintaining a constant Reynolds number of 150, the comparison ensures that the observed differences are solely due to the shape of the bodies and not influenced by varying flow conditions.
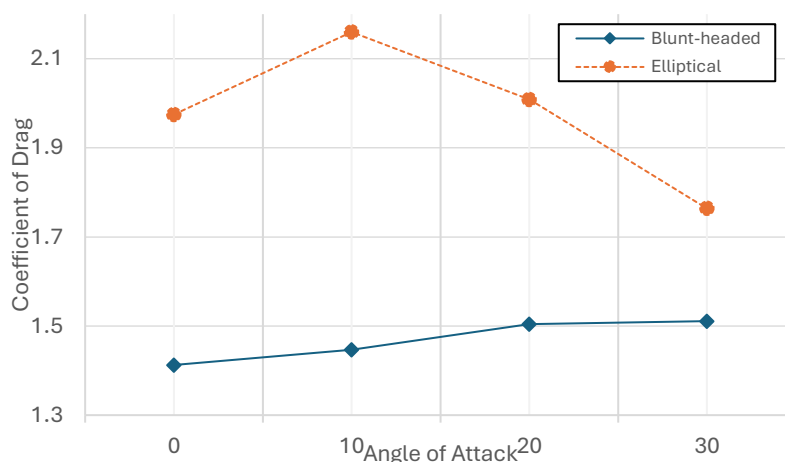
Fig. 8. Variation of Drag coefficient with Angle of attack for blunt-headed and elliptical bluff body

Figure 8 illustrates how the drag coefficient varies with the angle of attack for both blunt-headed and elliptical bluff bodies, with the Reynolds number set at 150. For the blunt-headed bluff body, the drag coefficient remains relatively stable across different angles of attack. At 0 degrees, the drag coefficient is about 1.4, and it experiences a slight increase to around 1.5 at 30 degrees. This consistency suggests that the blunt-headed bluff body's drag is relatively unaffected by changes in the angle of attack, maintaining a nearly constant profile. In contrast, the elliptical bluff body shows more pronounced changes in the drag coefficient as the angle of attack varies. Starting at approximately 1.9 at 0 degrees, the drag coefficient peaks at around 2.1 at 10 degrees before decreasing to about 1.8 at 30 degrees. This pattern indicates that the elliptical bluff body is more sensitive to changes in the angle of attack, with a significant increase in drag at moderate angles and a subsequent decrease at higher angles.

These differences are likely due to the unique geometries of the blunt-headed and elliptical bluff bodies, which affect how air flows around them. The blunt-headed body maintains a more consistent drag profile, while the elliptical body's drag coefficient fluctuates due to its shape influencing flow separation and reattachment differently at various angles of attack.

In summary, the graph demonstrates that while the blunt-headed bluff body maintains a steady drag coefficient across various angles of attack, the elliptical bluff body experiences a peak in drag at moderate angles followed by a decrease at higher angles. This behaviour highlights the distinct aerodynamic characteristics of each shape, adding depth to the previous analysis of their lift coefficients.

4.2 Strouhal Number

In figure 9 given below, the graph depicts the variation of the Strouhal number with the angle of attack for blunt-headed and elliptical bluff bodies, maintaining a constant Reynolds number of 150. As the angle of attack increases, the Strouhal number decreases for both types of bodies. At 0 degrees, the Strouhal number is about 0.4 for both blunt-headed and elliptical bodies. This value steadily drops to around 0.28 as the angle of attack reaches 30 degrees. The data reveals that despite the differing shapes, the Strouhal numbers for blunt-headed and elliptical bluff bodies remain almost identical across the tested angles, indicating that body shape has minimal impact on the Strouhal number under these conditions.
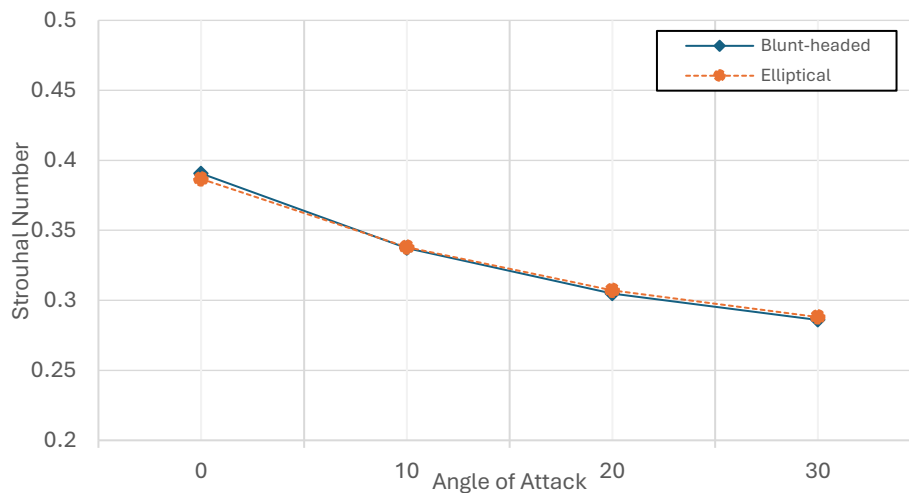

Fig. 9. Variation of Strouhal number with Angle of attack for blunt-headed and elliptical bluff body

The results for all the fluid flow parameters such as Lift Coefficient, Drag Coefficient and Strouhal Number are enlisted in Table 5.

Table 5. Result table for blunt-headed and elliptical bluff bodies at Re 150

	0°	10°	20°	30°
C_D (blunt-headed)	1.412549	1.446875	1.503879	1.511002
C_D (elliptical)	1.974751	2.159891	2.008825	1.763614
C_L (blunt-headed)	-0.001799	0.875475	1.557653	2.114523
C_L (elliptical)	0.002239	0.139708	0.270015	0.361173
Strouhal (blunt-headed)	0.390625	0.337211	0.304771	0.285963
Strouhal (elliptical)	0.386757	0.338086	0.307168	0.288050

4.3 Velocity and Pressure Contours

The velocity and pressure contours are analyzed for a Reynolds number of 150 at various angles of attack, providing crucial insights into the flow dynamics around the blunt cylinder. Here's a detailed explanation of the significance of each contour:

4.3.1 Velocity Contours

Velocity contours depict the flow velocities at different locations within the computational domain, offering a clear view of the flow pattern and velocity distribution around the blunt cylinder. These contours highlight regions of flow acceleration, deceleration, and flow separation, enabling the identification of critical flow features. They visually represent the flow structure, revealing the formation of vortices, wake regions, and boundary layer development. Understanding these velocity contours is vital for comprehending fluid dynamics aspects such as boundary layer behaviour, flow recirculation zones, and the interactions between the fluid and the blunt cylinder.

4.3.2 Pressure Contours

Pressure contours illustrate the distribution of pressure across the computational domain, highlighting areas of high and low pressure around the blunt cylinder. These contours are instrumental in visualizing how pressure gradients influence the flow pattern, with fluid moving from regions of high pressure to low pressure. Pressure contours can also indicate the presence of flow separation, variations in pressure along the cylinder's surface, and the formation of pressure gradients that affect the overall flow behaviour.

By thoroughly analyzing both velocity and pressure contours, one can gain a comprehensive understanding of the flow characteristics and fluid behaviour in the vicinity of the bluff bodies. This analysis is essential for elucidating the complex interactions and dynamics of the flow, providing valuable insights into the aerodynamic and hydrodynamic performance of the blunt cylinder. The following observations were made by comparing all the pressure, temperature, and velocity contours for both the blunt-headed and elliptical bodies, as shown in Figures 10-17.
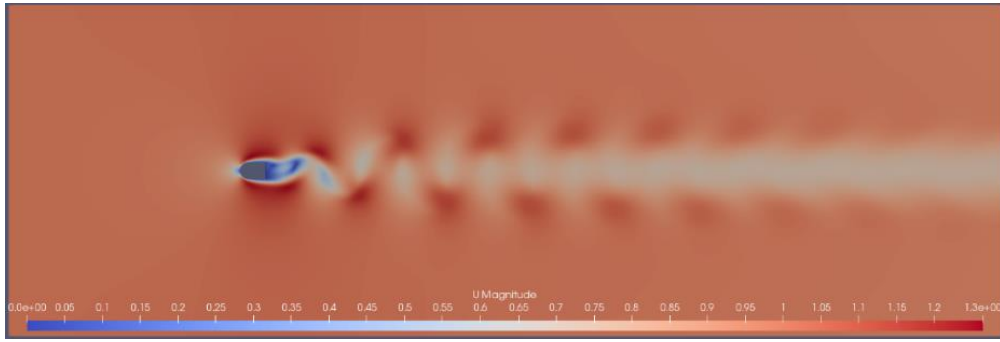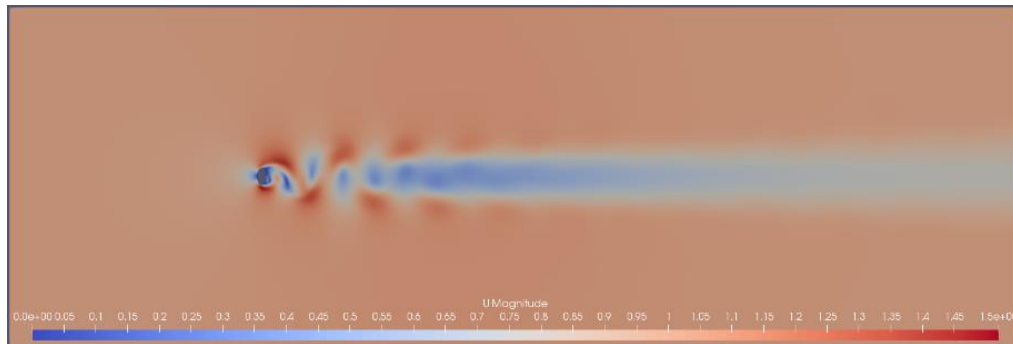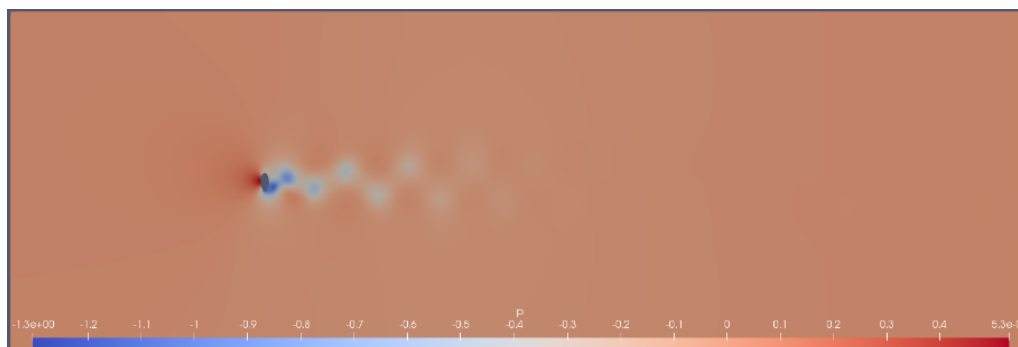
(a)
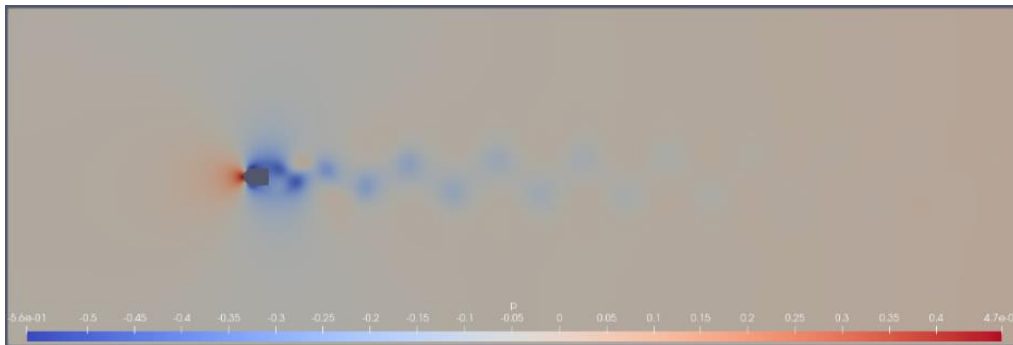
(b)

Fig. 10. (a) Velocity and (b) pressure contour of blunt-headed bluff body at 0° AOA
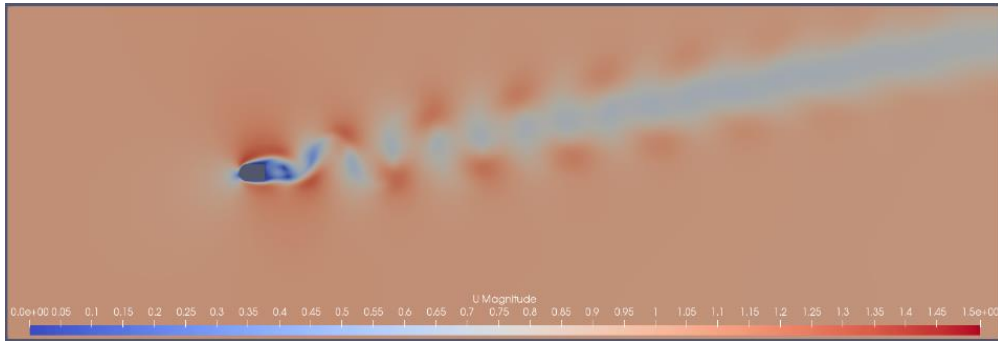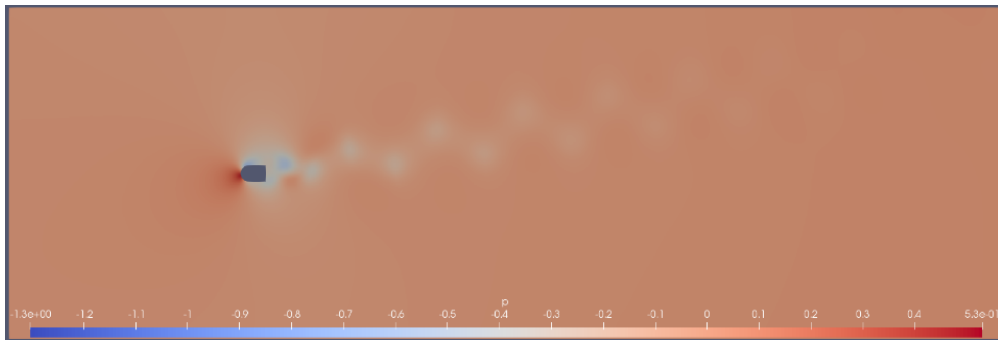

(a)

(b)

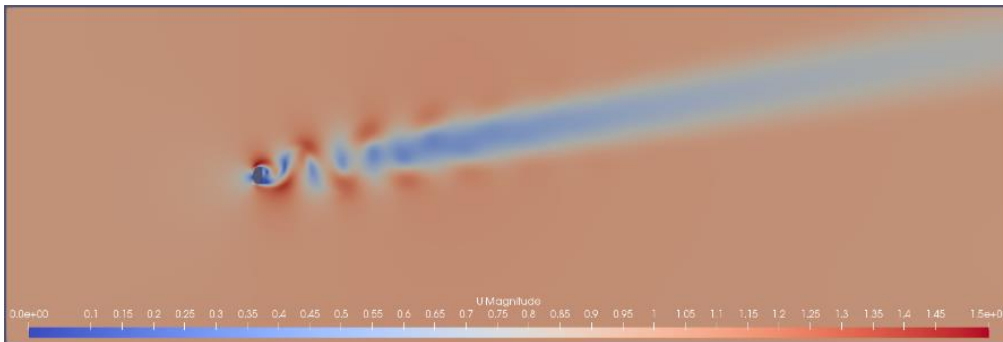Fig. 11. (a) Velocity and (b) pressure contour of elliptical bluff body at 0° AOA
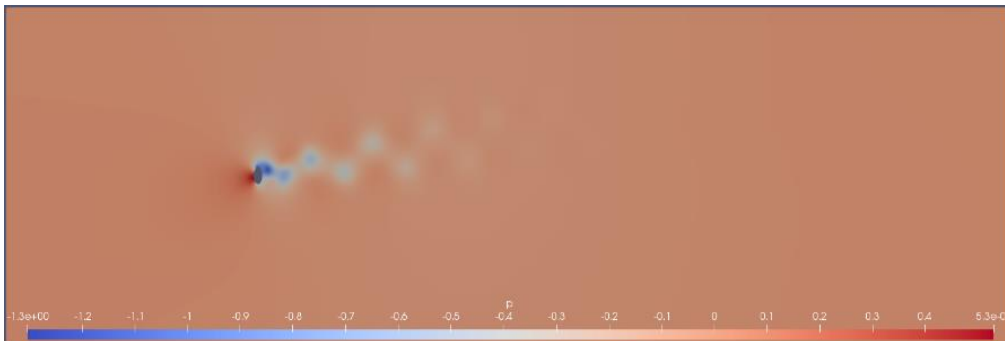
(a)

(b)

Fig. 12. (a) Velocity and (b) pressure contour of blunt-headed bluff body at 10° AOA
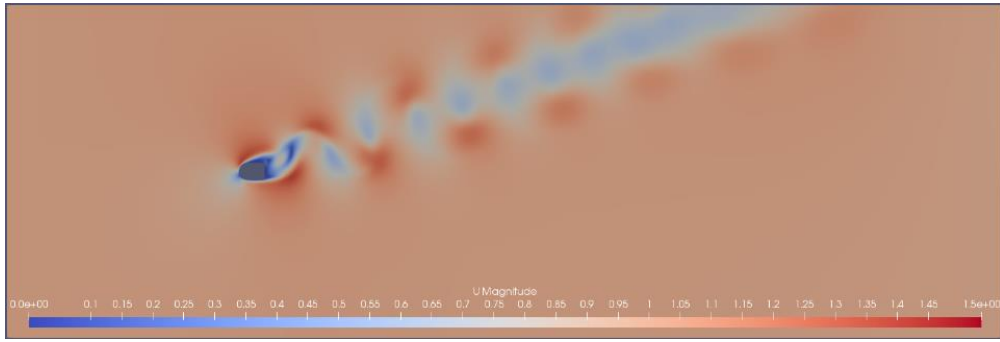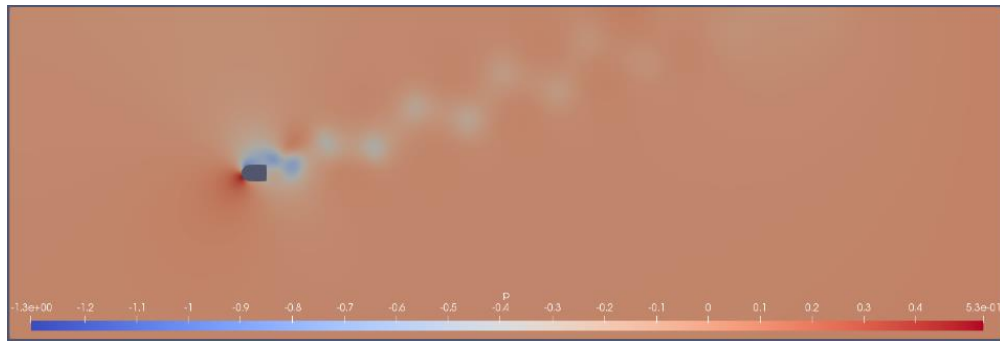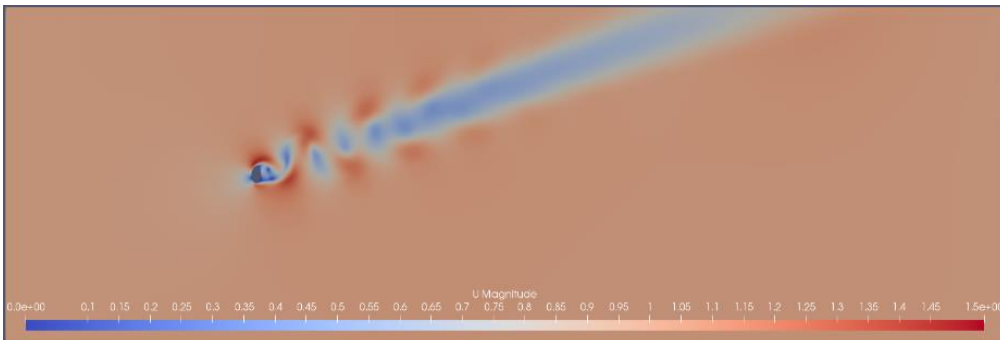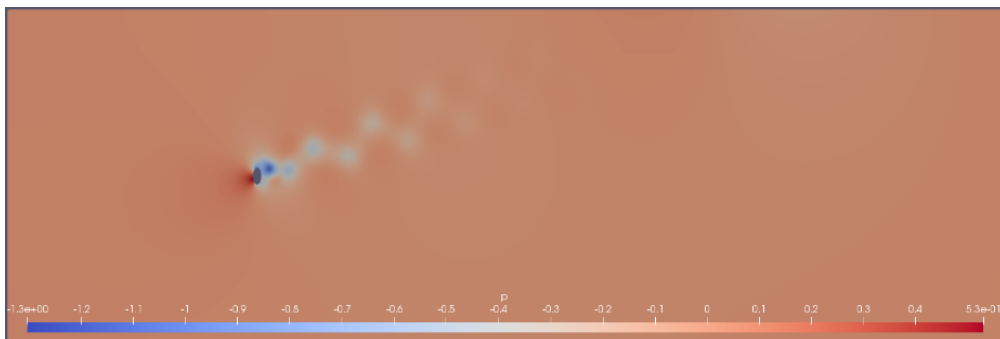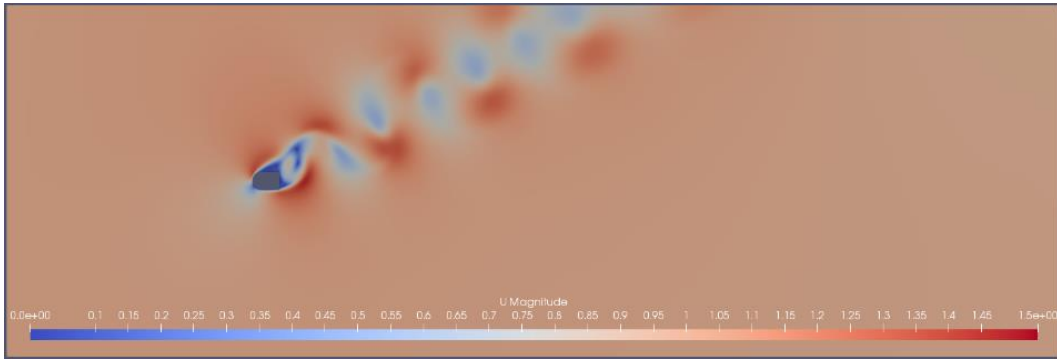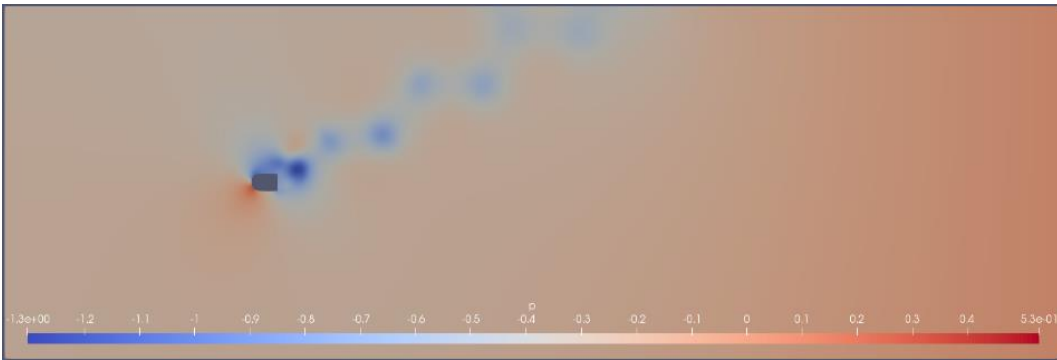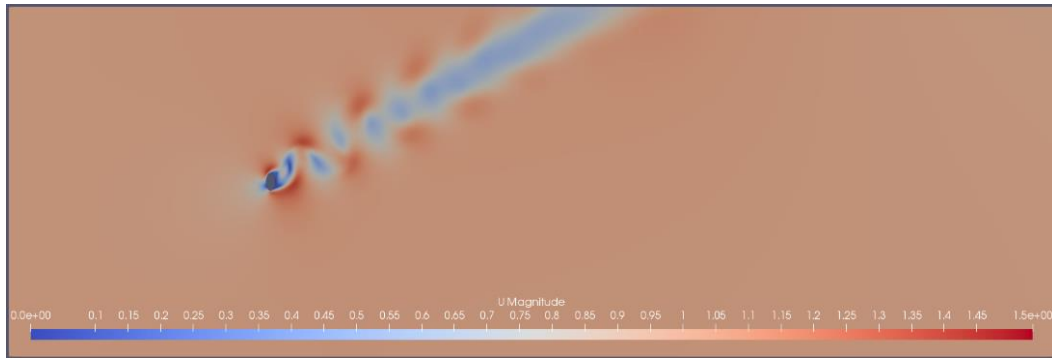

(a)

(b)

Fig. 13. (a) Velocity and (b) pressure contour of elliptical bluff body at 10° AOA

17

(a)

(b)

Fig. 14. (a) Velocity and (b) pressure contour of blunt-headed bluff body at 20° AOA

(a)

(b)

Fig. 15. (a) Velocity and (b) pressure contour of elliptical bluff body at 20° AOA
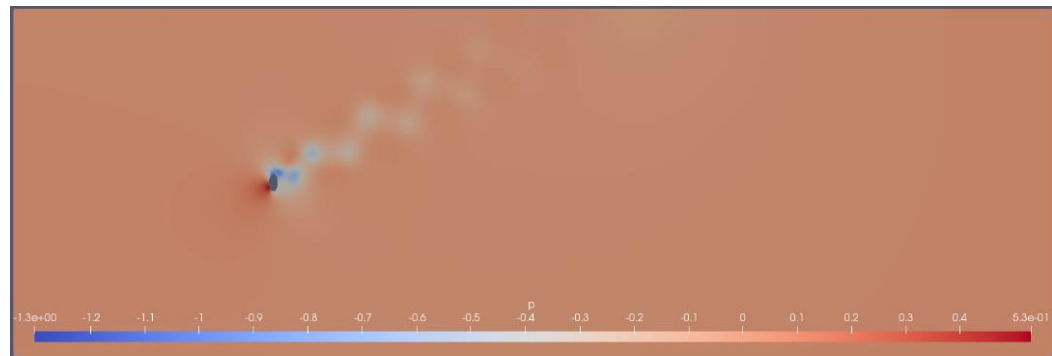
(a)

(b)

Fig. 16. (a) Velocity and (b) pressure contour of blunt-headed bluff body at 30° AOA

(a)

(b)

Fig. 17. (a) Velocity and (b) pressure contour of elliptical bluff body at 30° AOA

The following observations were made by comparing all the pressure, temperature, and velocity contours for both the blunt-headed and elliptical bodies.

Both the blunt-headed and elliptical bodies exhibit a high-pressure region on their front faces and a low-pressure region on their rear faces. As the angle of attack increases, the high-pressure region on the front face becomes more pronounced for both body types. Similarly, the low-pressure region on the rear face becomes more pronounced, shifting due to flow separation. At higher angles of attack, the pressure on the front face of both the blunt-headed and elliptical bodies increases because the flow becomes more turbulent, leading to greater pressure drag. Conversely, the pressure on the rear face decreases with increasing angles of attack, as flow separation creates a low-pressure wake region behind the bodies.

The velocity contours reveal high-velocity regions near the surface of both the blunt-headed and elliptical bodies and low-velocity regions in the surrounding fluid. As the angle of attack increases, the high-velocity region becomes wider and more intense for both body types, while the low-velocity region also expands and intensifies. With increasing angles of attack, the fluid velocity increases due to the higher kinetic energy associated with turbulent flow. Additionally, the velocity near the surface of both bodies rises as the boundary layer velocity increases with the angle of attack.

4.4 Variation of C_D and C_L with time

Analyzing the variations of lift (C_L) and drag (C_D) coefficients over time is crucial for evaluating aerodynamic performance, flow stability, and unsteadiness. These coefficients offer valuable insights into the interaction between the cylinder and the flow, as well as its aerodynamic efficiency. At higher angles of attack, fluctuations in Cl and Cd are indicative of flow unsteadiness and turbulence, primarily due to vortex shedding in the wake region. This analysis is essential for optimizing aerodynamic designs and ensuring stable performance under varying flow conditions.
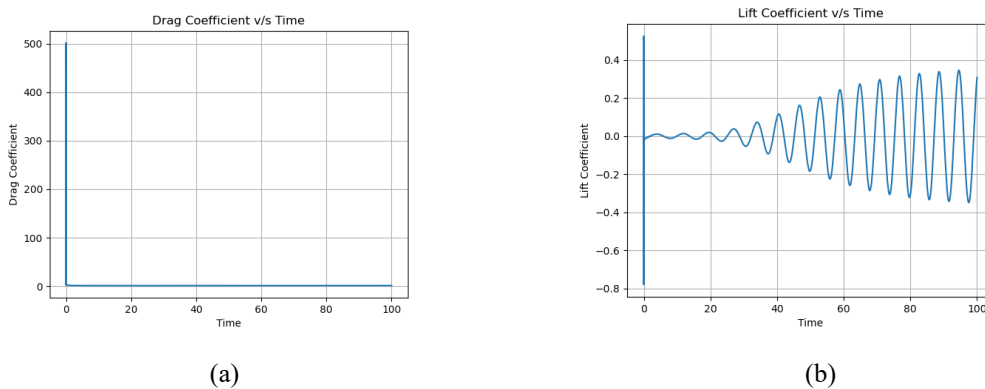

(a)   (b)

Fig. 18. Variation of (a) C_D and (b) C_L for blunt-headed bluff body at 0° AOA
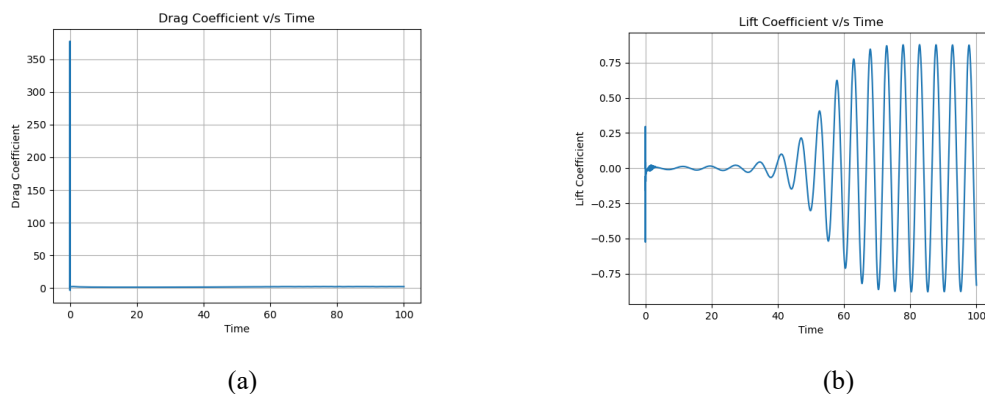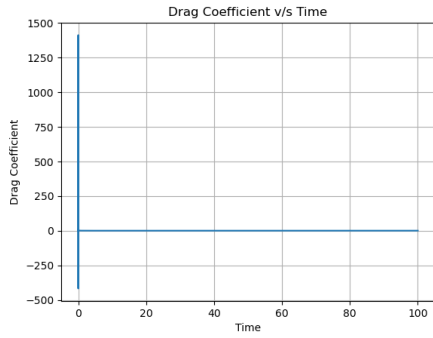

(a)   (b)

Fig. 19. Variation of (a) C_D and (b) C_L for elliptical bluff body at 0° AOA

Fig. 20. Variation of (a) C_D and (b) C_L for blunt-headed bluff body at 10° AOA
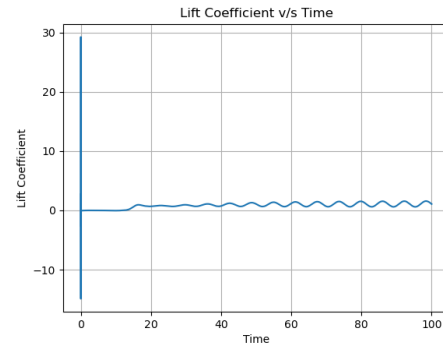

Fig. 21. Variation of (a) C_D and (b) C_L for elliptical bluff body at 10° AOA

Fig. 22. Variation of (a) C_D and (b) C_L for blunt-headed bluff body at 20° AOA

(a)   (b)

Fig. 23. Variation of (a) C_D and (b) C_L for elliptical bluff body at 20° AOA

(a)   (b)
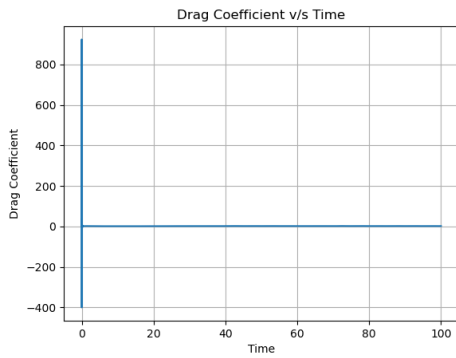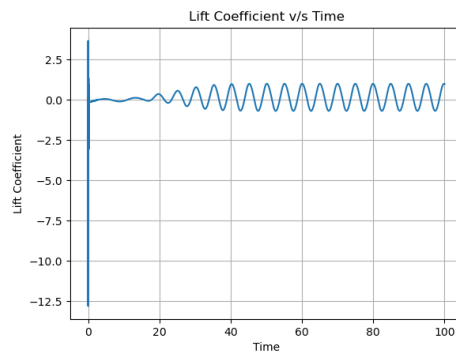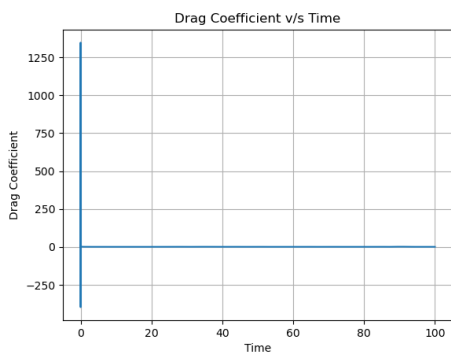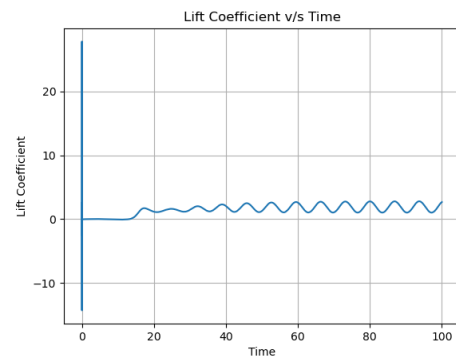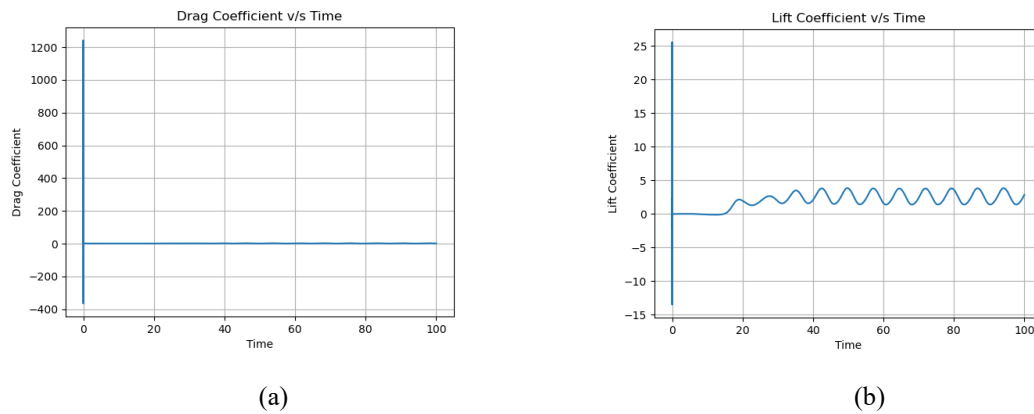
Fig. 24. Variation of (a) C_D and (b) C_L for blunt-headed bluff body at 30° AOA
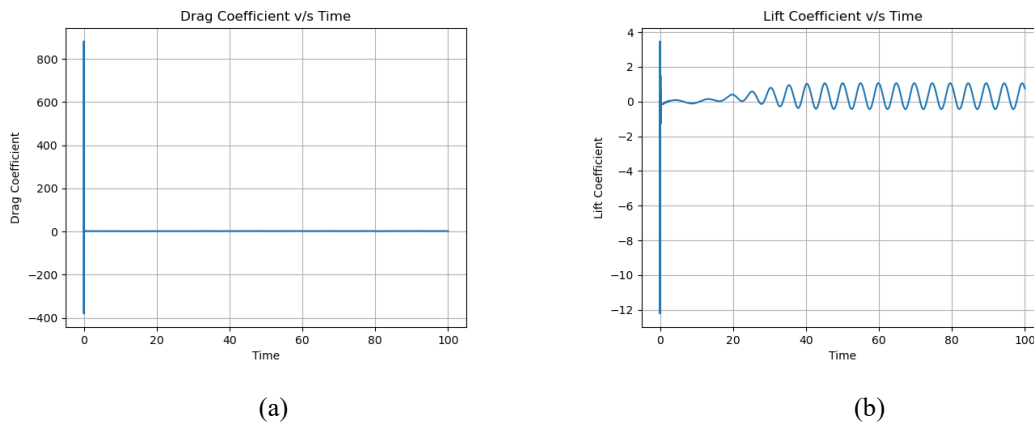

(a)   (b)
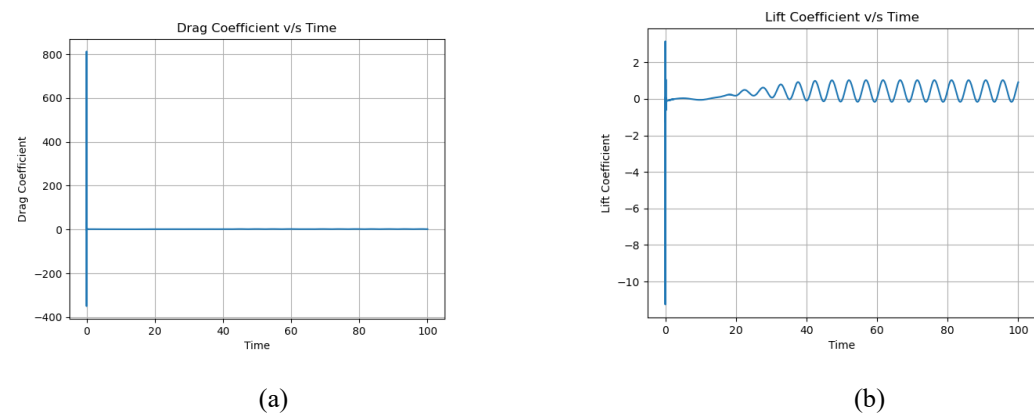
Fig. 25. Variation of (a) C_D and (b) C_L for elliptical bluff body at 30° AOA

4.5 Frequency Analysis

The Fast Fourier Transform (FFT) analysis is a powerful tool for breaking down the lift signal into its individual frequency components. By applying the FFT algorithm, one can generate a plot that displays the energy distribution across various harmonics of the signal. The harmonics with the highest energy levels represent the dominant frequencies within the lift signal. From this FFT plot, the dominant frequency can be identified, allowing for the calculation of the Strouhal number (St). The Strouhal number is a dimensionless quantity that links the shedding frequency of vortices in the wake of the blunt cylinder to the characteristic flow velocity and the

characteristic length of the body. This analysis provides critical insights into the flow dynamics and vortex shedding behaviour, which are essential for understanding and optimizing aerodynamic performance.

(a)

(b)

Fig. 26. Variation of amplitude to frequency for (a) blunt-headed and (b) elliptical bluff body at 0° AOA

(a)

(b)

Fig. 27. Variation of amplitude to frequency for (a) blunt-headed and (b) elliptical bluff body at 10° AOA

(a)

(b)

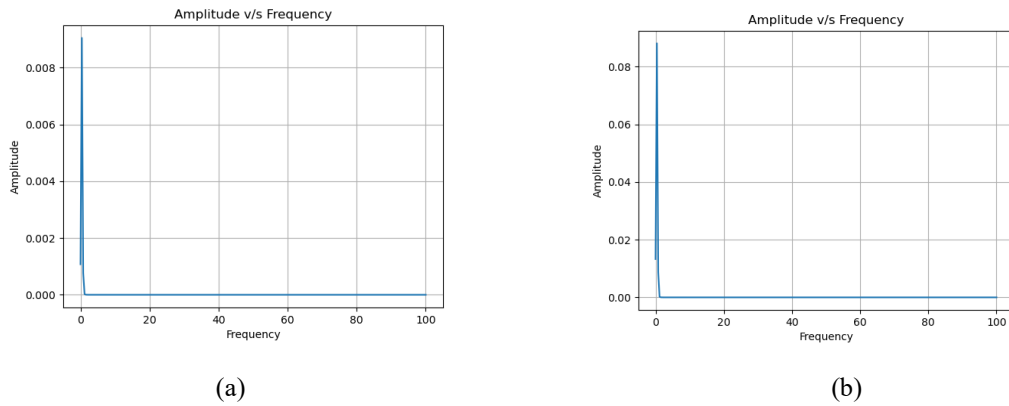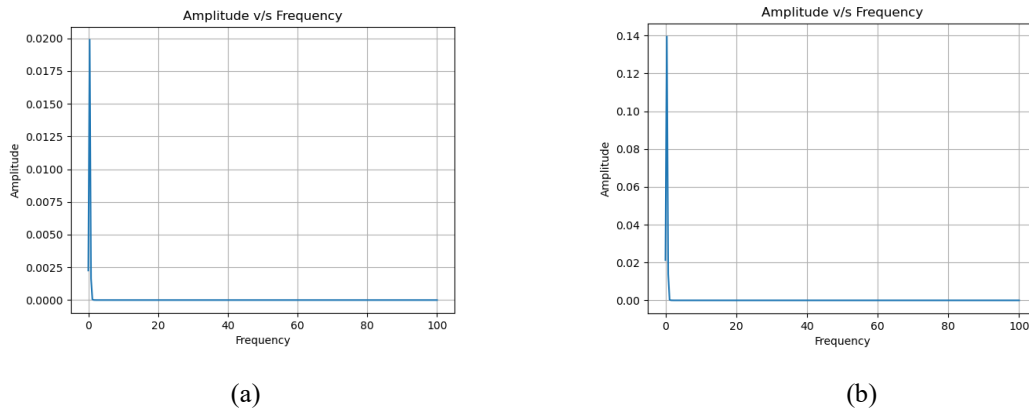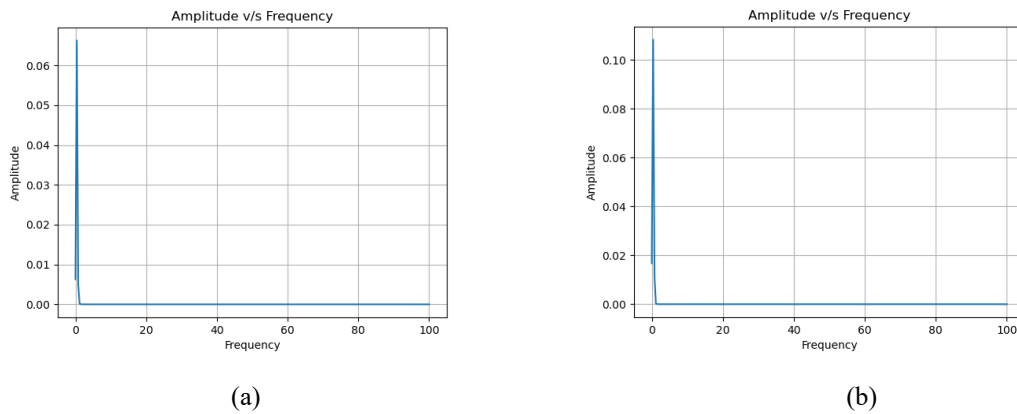Fig. 28. Variation of amplitude to frequency for (a) blunt-headed and (b) elliptical bluff body at 20° AOA

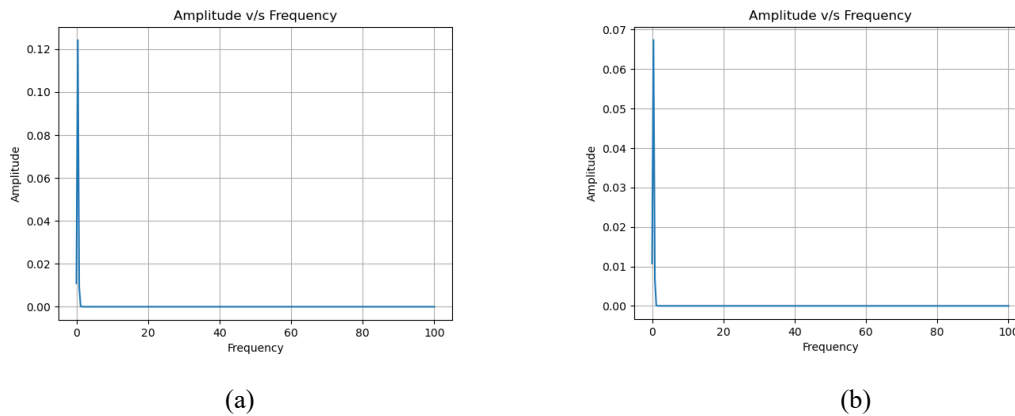(a)   (b)

Fig. 29. Variation of amplitude to frequency for (a) blunt-headed and (b) elliptical bluff body at 30° AOA

The technical interpretation of this result indicates that as the angle of attack increases, the flow dynamics change, leading to variations in the shedding frequency of vortices in the wake region. For the blunt-headed bluff body, the frequency shows a steady increase with the angle of attack. This suggests a direct correlation between the flow dynamics and the angle of attack, with the flow becoming more turbulent and the vortex shedding occurring at higher frequencies as the angle of attack increases.

Conversely, for the elliptical body, the frequency demonstrates a steady decrease with increasing angle of attack. This behaviour is indicative of different aerodynamic characteristics and flow interactions compared to the blunt-headed bluff body. The linear relationship between frequency and angle of attack for both body types suggests that the angle of attack significantly influences the vortex-shedding behaviour, albeit in opposite manners.

The slight fluctuations observed in the frequency curves can be attributed to the inherent variability in the flow field and the complex interactions between the flow and the bodies. Factors such as flow instabilities, boundary layer effects, and vortex interactions may contribute to these fluctuations. Nonetheless, the overall trends indicate that as the angle of attack increases, the vortex shedding frequency increases for the blunt-headed body and decreases for the elliptical body, reflecting their distinct aerodynamic responses to changes in the flow conditions.

5. Conclusion

The numerical analysis of flow over a blunt-headed body and an elliptical body using PISOFOAM in OpenFOAM has yielded valuable insights into flow behaviour. The simulation results, presented through pressure and velocity contours, provided detailed visual representations of the flow field, enhancing our understanding of the spatial distribution and dynamics of these parameters.

The study focused on analyzing the lift (C_L) and drag (C_D) coefficients over time for a Reynolds number of 150. The results indicated that at lower angles of attack, these coefficients remained constant, signifying a steady flow regime. However, at higher angles of attack, fluctuations were observed in both C_L and C_D, indicating an unsteady flow attributed to vortex shedding in the wake region.

To delve deeper into the vortex shedding phenomenon, a Fast Fourier Transform (FFT) analysis was conducted on the lift signal, identifying the dominant shedding frequency. This frequency was used to calculate the Strouhal number (St), which relates the shedding frequency to the flow parameters. The analysis revealed that the Strouhal number decreased with an increase in the angle of attack, highlighting the intricate relationship between flow dynamics and geometric orientation.

In conclusion, while lower Reynolds number flows could be successfully analyzed, attempts to simulate moderate to high Reynolds number flows were hindered by the limitations of the PISOFOAM solver in OpenFOAM, resulting in solver crashes when validating the results of the literature [5]. Future research may require more advanced solvers or alternative computational approaches to effectively study high Reynolds number flows and capture the complex flow dynamics around bluff bodies.

References

[1]   Chourushi, T., A. Rahimi, S. Singh, and R. S. Myong, "Computational simulations of near-continuum gas flow using Navier-Stokes-Fourier equations with slip and jump conditions based on the modal discontinuous Galerkin method." In *Advances in Aerodynamics 2* (2020): 1-37.

[2]   Yuce M, Kareem D, "A Numerical Analysis Of Fluid Flow Around Circular And Square Cylinders". In *American Water Works Association* (2016). DOI: 108(10) E546-E554

[3]   Chatterjee D, Gupta S, "Numerical Study Of The Laminar Flow Past A Rotating Square Cylinder At Low Spinning Rates". *In Journal of Fluids Engineering, Transactions of the ASME* (2015). DOI: 10.1115/1.4028500

[4]   Chevula S, "Aerodynamic Loads On Bluff Bodies Under Wind Gusts". In *Instituto de Microgravedad "Ignacio Da Riva"* (2015). DOI: 10.13140/RG.2.2.21970.96967

[5]   Wang S, Cheng W, Du R, Wang Y, "Unsteady RANS Modeling Of Flow Around Two-Dimensional Rectangular Cylinders With Different Side Ratios At Reynolds Number 6.85×10^5". In *Mathematical Problems in Engineering* (2020). DOI: 10.1155/2020/2163928

[6]   Website: https://github.com/meinarsve/CFDwOpenFoam/blob/master/squareCylinder_kEpsilon/-turbulenceModels.pdf, *as per the website access on 27 June 2024*.

[7]   H.G. Weller, G. Tabor, H. Jasak, C. Fureby, "A tensorial approach to computational continuum mechanics using object-oriented techniques". In *Computers in Physics*. DOI: 12(6), 620 -631, 1998.

[8]   T. Chourushi, "A High-Resolution Equi-Gradient scheme for convective flows." *In Applied Mathematics and Computation*. DOI: 338, 123-140, 2018.

[9]   T. Chourushi, "Effect of fluid elasticity on the numerical stability of high-resolution schemes for high shearing contraction flows using OpenFOAM", In *Theoretical and Applied Mechanics Letters*. DOI: 7(1), 41-51, 2017.

[10]   H. K. Versteeg, "An introduction to computational fluid dynamics the finite volume method", In *2nd Edition. Pearson Education India* (2007).

Annexure – 1: Mesh quality report for blunt-headed bluff body

```
/*---------------------------------------------------------------------------*\
  =========                 |
  \\      /  F ield         | OpenFOAM: The Open Source CFD Toolbox
   \\    /   O peration     | Website:  https://openfoam.org
    \\  /    A nd           | Version:  9
     \\/     M anipulation  |
\*---------------------------------------------------------------------------*/
Build  : 9-c96968adf6d8
Exec   : checkMesh
Date   : Jun 27 2024
Time   : 13:31:39
Host   : "EVAN"
PID    : 1642
I/O    : uncollated
Case   : /home/infinity/internship/test_cases/cases/TC02A
nProcs : 1
sigFpe : Enabling floating point exception trapping (FOAM_SIGFPE).
fileModificationChecking : Monitoring run-time modified files using timeStampMaster (fileModificationSkew 10)
allowSystemOperations : Allowing user-supplied system call operations

// * * * * * * * * * * * * * * * * * * * * * * * * * * * * * * * * * * * * * //
Create time

Create polyMesh for time = 0

Time = 0

Mesh stats
    points:           74520
    internal points:  0
    faces:            147660
    internal faces:   73140
    cells:            36800
    faces per cell:   6
    boundary patches: 5
    point zones:      0
    face zones:       0
    cell zones:       0

Overall number of cells of each type:
    hexahedra:     36800
    prisms:        0
    wedges:        0
    pyramids:      0
    tet wedges:    0
    tetrahedra:    0
    polyhedra:     0

Checking topology...
    Boundary definition OK.
    Cell to face addressing OK.
    Point usage OK.
    Upper triangular ordering OK.
    Face vertices OK.
    Number of regions: 1 (OK).

Checking patch topology for multiply connected surfaces...
    Patch            Faces    Points   Surface topology
    cylinder         280      560      ok (non-closed singly connected)
    symmetry         480      964      ok (non-closed singly connected)
    inlet            80       162      ok (non-closed singly connected)
    outlet           80       162      ok (non-closed singly connected)
    frontAndBackPlanes 73600  74520    ok (non-closed singly connected)

Checking geometry...
    Overall domain bounding box (13.398 17.61 -0.632456) (73.398 37.61 0.632456)
    Mesh has 2 geometric (non-empty/wedge) directions (1 1 0)
    Mesh has 2 solution (non-empty) directions (1 1 0)
    All edges aligned with or perpendicular to non-empty directions.
    Boundary openness (6.39366e-19 -1.07627e-18 -6.66007e-20) OK.
    Max cell openness = 2.95808e-16 OK.
    Max aspect ratio = 6.40251 OK.
    Minimum face area = 0.000282758. Maximum face area = 0.777079.  Face area magnitudes OK.
    Min volume = 0.000357663. Max volume = 0.236226.  Total volume = 1517.4.  Cell volumes OK.
    Mesh non-orthogonality Max: 59.6115 average: 23.0536
    Non-orthogonality check OK.
    Face pyramids OK.
    Max skewness = 1.97311 OK.
    Coupled point location match (average 0) OK.

Mesh OK.

End
```

Annexure – 2: Mesh quality report for elliptical bluff body

```
/*---------------------------------------------------------------------------*\
  =========                 |
  \\      /  F ield          | OpenFOAM: The Open Source CFD Toolbox
   \\    /   O peration       | Website:  https://openfoam.org
    \\  /    A nd             | Version:  9
     \\/     M anipulation    |
\*---------------------------------------------------------------------------*/
Build  : 9-c96968adf6d8
Exec   : checkMesh
Date   : Jun 27 2024
Time   : 13:31:39
Host   : "EVAN"
PID    : 1642
I/O    : uncollated
Case   : /home/infinity/internship/test_cases/cases/TC02A
nProcs : 1
sigFpe : Enabling floating point exception trapping (FOAM_SIGFPE).
fileModificationChecking : Monitoring run-time modified files using timeStampMaster (fileModificationSkew 10)
allowSystemOperations : Allowing user-supplied system call operations

// * * * * * * * * * * * * * * * * * * * * * * * * * * * * * * * * * * * * * //
Create time

Create polyMesh for time = 0

Time = 0

Mesh stats
    points:           74520
    internal points:  0
    faces:            147660
    internal faces:   73140
    cells:            36800
    faces per cell:   6
    boundary patches: 5
    point zones:      0
    face zones:       0
    cell zones:       0

Overall number of cells of each type:
    hexahedra:     36800
    prisms:        0
    wedges:        0
    pyramids:      0
    tet wedges:    0
    tetrahedra:    0
    polyhedra:     0

Checking topology...
    Boundary definition OK.
    Cell to face addressing OK.
    Point usage OK.
    Upper triangular ordering OK.
    Face vertices OK.
    Number of regions: 1 (OK).

Checking patch topology for multiply connected surfaces...
    Patch                   Faces    Points    Surface topology
    cylinder                280      560       ok (non-closed singly connected)
    symmetry                480      964       ok (non-closed singly connected)
    inlet                   80       162       ok (non-closed singly connected)
    outlet                  80       162       ok (non-closed singly connected)
    frontAndBackPlanes      73600    74520     ok (non-closed singly connected)

Checking geometry...
    Overall domain bounding box (13.398 17.61 -0.632456) (73.398 37.61 0.632456)
    Mesh has 2 geometric (non-empty/wedge) directions (1 1 0)
    Mesh has 2 solution (non-empty) directions (1 1 0)
    All edges aligned with or perpendicular to non-empty directions.
    Boundary openness (6.39366e-19 -1.07627e-18 -6.66007e-20) OK.
    Max cell openness = 2.95808e-16 OK.
    Max aspect ratio = 6.40251 OK.
    Minimum face area = 0.000282758. Maximum face area = 0.777079.  Face area magnitudes OK.
    Min volume = 0.000357663. Max volume = 0.236226.  Total volume = 1517.4.  Cell volumes OK.
    Mesh non-orthogonality Max: 59.6115 average: 23.0536
    Non-orthogonality check OK.
    Face pyramids OK.
    Max skewness = 1.97311 OK.
    Coupled point location match (average 0) OK.

Mesh OK.

End
```

Annexure – 3: Python code to generate Strouhal number

```python
#!/usr/bin/python3
import numpy as np
import scipy.signal as signal
import matplotlib.pyplot as plt

# Read Results
data = np.loadtxt('./postProcessing/forceCoeffs/0/forceCoeffs.dat', skiprows=0)
L = 1 # L = D - Diameter
V = 1 # Velocity
time = data[:,0]
Cd = data[:,2]
Cl = data[:,3]
del data

# Compute FFT
N = len(time)
dt = time[2] - time[1]

# Better stable FFT
nmax = 512 # no. of points in the fft
freq, Cd_amp = signal.welch(Cd, 1./dt, nperseg=nmax)
freq, Cl_amp = signal.welch(Cl, 1./dt, nperseg=nmax)

plt.plot(freq, Cl_amp)
plt.grid()
plt.title("Amplitude v/s Frequency")
plt.xlabel("Frequency")
plt.ylabel("Amplitude")
plt.show()

# Strouhal Number
# Find the index corresponding to max amplitude
Cl_max_fft_idx = np.argmax(abs(Cl_amp))
freq_shed = freq[Cl_max_fft_idx]
St = freq_shed * L / V
print("Vortex shedding freq: %.6f [Hz]" % (freq_shed))
print("Strouhal Number: %.6f" % (St))

# Time v/s Lift Coefficient
plt.plot(time, Cl)
plt.grid()
plt.title("Lift Coefficient v/s Time")
plt.xlabel("Time")
plt.ylabel("Lift Coefficient")
plt.show()
```

```python
# Time v/s Drag Coefficient
plt.plot(time, Cd)
plt.grid()
plt.title("Drag Coefficient v/s Time")
plt.xlabel("Time")
plt.ylabel("Drag Coefficient")
plt.show()

# Calculate average after stabilization
stabilization_period = 1000 # Choose an appropriate stabilization period
avg_Cl = np.mean(Cl[stabilization_period:])
avg_Cd = np.mean(Cd[stabilization_period:])

print("Average Lift Coefficient after stabilization:", avg_Cl)
print("Average Drag Coefficient after stabilization:", avg_Cd)
```